Mechanical performance of bamboo-inspired tapered hollow strut lattice structures fabricated by laser powder bed fusion (LPBF)

Yu Song[1],[†], Zhenyu Chen[1],[†], Tongzheng Wei[1], Chen Ge[1], Yuang Cheng[1], Ming Liu[2],* and Qingbo Jia[1],*

[1] School of Mechanical and Electrical Engineering, Soochow University, Suzhou 215131, China

[2] State Key Laboratory of Electromechanical Integrated Manufacturing of High-performance Electronic Equipments, Xidian University, Xi'an 710071, China

[†] These authors contributed equally to this work.

* Correspondence authors; E-mails: qbjia@suda.edu.cn (Q. J.); ming.liu@xidian.edu.cn (M. L.).

Abstract: Drawing upon the intricacies of nature, bionics has significantly bolstered the engineering structure performance by providing innovative solutions and novel design principles. This study presented a tapered hollow strut lattice structure design that is inspired by the unique structural attributes of bamboo. The relative density, mechanical responses and Zenner's anisotropy of the developed BCC, RD and OCTET unit cells with tapered hollow struts were simulated, while the corresponding geometric configurations that deliver the best combinations of physical and mechanical properties were optimized. The selected unit cells were then fabricated into $3 \times 3 \times 3$ type lattice structures by laser powder bed fusion (LPBF) for experimental analysis. The compression results confirmed that the tapered hollow strut design obviously improved the deformation stability as compared with the straight hollow strut and solid strut design counterparts. Deformation modes analysis suggested that the tapered hollow strut design enhanced the strength and shear resistance, which contributed to the deformation stability improvement of the designed lattice structure. The current study is envisaged to provide useful guidance for future bio-inspired lattice structure design, with the final aim of enhancing the mechanical properties of the lightweight components.

Keywords: laser powder bed fusion; additive manufacturing; hollow strut lattice structure; compression strength; energy absorption

1. Introduction

Over the last decades, scientists have been deriving inspirations from intricate yet predictable traits of natural substances to develop materials and structures that can surpass their natural equivalents. Artificial cellular materials, which are designed to mimic wood and cancellous bone, are now considered the most promising lightweight multifunctional materials for aerospace, biomedical, construction and automotive applications [1–3]. In general, these cellular structures can be divided into stochastic and periodic foam structures depending on the randomness of the internal pores. Herein, the former has a unit shape and distribution pattern that is spatially random, whereas the latter consists of topologically organized repeating unit cells, such as the commonly known lattice structures [4]. The smallest constituent units of the lattice structure, namely the unit cell, is determined by the proportions and connections of their individual strut elements, which are linked at particular nodes. At the cellular level, lattice structures exhibit traits and qualities of structures, while they function as homogenized metamaterials at the overall structural level [5].

With the ever-improving manufacturing capabilities provided by laser powder bed fusion (LPBF), researchers can now easily design and fabricate novel metallic lattice structures with attractive physical properties, including acoustic, dielectric and mechanical properties [6,7]. For example, Qi et al. [8] fabricated the lattice structures composed of octet-truss and truncated-octahedron unit cells with both regular and tapered beams through LPBF, respectively. The designed structure showed significant enhancement of elastic modulus as compared with its original counterparts. Xiao et al. [9] proposed a hybrid lattice structure, combining the benefits of both bending-dominated rhombic dodecahedron and stretching-dominated octet cells, and such hybrid structure presented a high initial strength and smooth post-yielding response, making it an appropriate candidate for energy absorption. Zhang et al. [10] developed a gradient lattice structure in topology to achieve adjustable mechanical performance, and both experimental and numerical simulation results demonstrated its superior stiffness and energy absorption capacity than the classical BCC lattice structures.

Among all the artificial cellular structures, the bio-inspired lattice structure is now gaining the most popularity due to the hierarchical structures inherent to the biological systems, which dramatically improved its functional performance [11,12]. On such basis, researchers tried to additively manufacture diverse lattice structures inspired by biological systems to achieve specific mechanical property enhancements for various engineering applications [13]. Sharma et al. [14] designed a novel lattice structure inspired by euplectella aspergillum, and it was found the strut thickness, relative density and unit cell size have significant influence on energy absorption and deformation behaviors. Jia et al. [15] presented the design of a unique dual-scale single crystalline structure observed in starfish ossicles, which demonstrated outstanding strength, toughness and damage tolerance. Inspired by the sea urchin, Kumar et al. [16] conducted the research on a bio-inspired closed lattice structure and found that the stiffness improved by about 25% in comparison to the open-cell lattice structure counterparts. Li et al. [17] introduced a biomimetic lattice structure with variable cross-sectional dimensions inspired by the shape of starfruit, and the corresponding

compression performance and energy absorption efficiency of the presented structure were evaluated using non-axial compression experiments and simulations.

As one of the commonly studied biological organisms, bamboo with a lightweight structure feature displays exceptional mechanical performance, especially for withstanding the heavy wind and/or snow induced high bending stress [18]. The hollow structures of the bamboo enhance the inertia moment of the struts that significantly reduces the magnitude of the bending stress. Moreover, the bamboo node plays a key role in resisting lateral shear and improving stress dissipation caused by compressive loads [19]. On such basis, research efforts have been focused on integrating the structural features of bamboo to enhance the axial/lateral strength and the energy absorption behaviors of the thin-wall tubes [20,21], including replicating the hollow structure of bamboo with various outer shapes/uniform inner cross-sections. For example, Miao *et al.* [22] explored the elastic modulus, shear modulus, mechanical property anisotropy and deformation behavior of bamboo-inspired BCC lattice structure with hollow and tapered struts. Li *et al.* studied the effects of geometric parameters on axial compression performance of a bamboo-inspired porous lattice structure [23]. Nevertheless, most of the previous researches examined the performance of the designed structures that primarily mimicked the exterior configurations of the bamboo, while the extensive possibilities of its topological nature still worth further explorations.

Inspired by the biological feature of the bamboo cross-section, we have developed a new type of tapered hollow strut lattice structure design in our previous work, in which the geometrical parameter effects on mechanical performance were systematically evaluated [24]. This study is mainly aimed to extend and verify the design strategy in other types of lattice constructions and more importantly, compare its mechanical properties with its commonly studied solid strut and hollow strut counterparts. Specifically, the mechanical properties, the deformation behaviors and the failure modes of such lattice structures were systematically investigated. This paper is organized as follows. Section 2 introduces the design map, numerical optimization, fabrication methods and experimental testing of the developed lattice structures. Section 3 presents the numerically simulated and experimentally measured results, in which the mechanical performance and deformation modes of the tapered hollow strut, straight hollow strut as well as the solid strut lattice structures are discussed. Section 4 concludes the key findings of the present study.

2. Materials and methods

2.1. Design strategy of tapered hollow strut unit cell

The structure of bamboo exemplifies an efficient lightweight design that combines low density and excellent mechanical properties. The typical geometric structure of bamboo consists of hollow and gradually narrowing pillars (along the growing direction) that are connected by nodes, as demonstrated in Figure 1. Taking inspiration from the cross-sectional geometry of bamboo, we substituted the unit cell's solid struts with tapered hollow struts while maintaining the outer diameter of the struts unchanged. To achieve this structure design, we initially developed two tapered solid struts: tapered away from the node (TAN)

and tapered towards the node (TTN), based on the taper's directional flow in relation to the node. Herein, the top radius r_{top} is larger for TAN and smaller for TTN as compared with the node radius r_{node}. The next step involves replacing the solid straight struts of the typical BCC, octet-truss, and RD structures with the TAN and TTN tapered struts. The final step is the construction of three categories of tapered hollow strut unit cells by subtracting the uniform cross-section of the solid struts from their TAN and TTN equivalents. Alterations in the top and bottom radius of cells in the TTN group align with those in the TAN group, which guarantees the equivalence of absolute difference between the r_{top} and r_{node} in each pair of cases. As a result, a design matrix of tapered hollow strut unit cells can be created for mechanical property optimization by modifying the geometric parameters (e.g. r_{top} and r_{node}) of each type of lattice structures. Herein, the geometrical dimension of the hollow strut should prevent powder occlusion while ensuring an adequate strut wall thickness during the LPBF fabrication process. These aspects will be discussed in detail in the subsequent section.
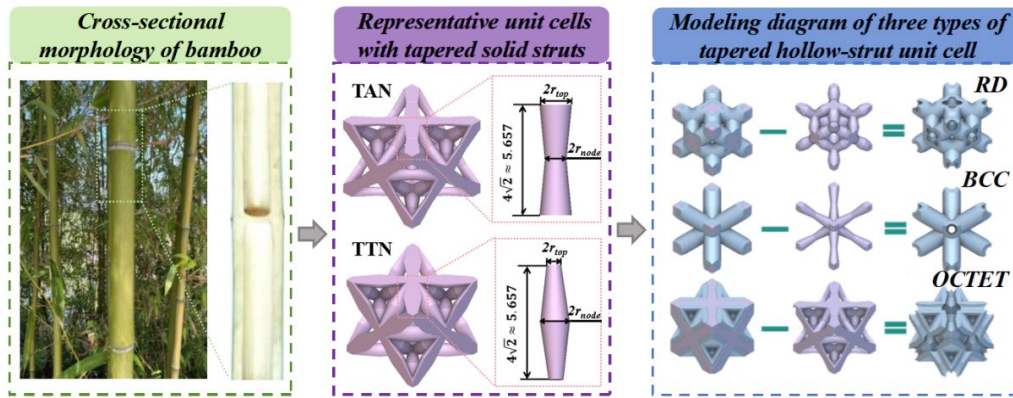

Figure 1. Design strategy of the bamboo-inspired tapered hollow strut structures.

2.2. Tapered hollow strut structure optimization and numerical simulation

The geometrical parameter effects on mechanical performance of the developed lattice structures were simulated, using the representative volume element (a unit cell) model method. The periodic boundary conditions were applied to every two opposite surfaces of the unit cell, and the elastic property analysis was performed in the COMSOL environment. Due to its inherent cubic symmetry, the elastic tensor of three independent components of C_{11}, C_{12} and C_{44} was calculated according to the following matrix [25]:

$$\begin{pmatrix} \sigma_{11} \\ \sigma_{22} \\ \sigma_{33} \\ \sigma_{23} \\ \sigma_{12} \\ \sigma_{13} \end{pmatrix} = \begin{pmatrix} C_{11} & C_{12} & C_{12} & 0 & 0 & 0 \\ C_{12} & C_{11} & C_{12} & 0 & 0 & 0 \\ C_{12} & C_{12} & C_{11} & 0 & 0 & 0 \\ 0 & 0 & 0 & C_{44} & 0 & 0 \\ 0 & 0 & 0 & 0 & C_{44} & 0 \\ 0 & 0 & 0 & 0 & 0 & C_{44} \end{pmatrix} \begin{pmatrix} \varepsilon_{11} \\ \varepsilon_{22} \\ \varepsilon_{33} \\ \varepsilon_{23} \\ \varepsilon_{12} \\ \varepsilon_{13} \end{pmatrix} \qquad (1)$$

Herein, the stress, strain as well as the shear modulus values in the matrix were obtained from compression simulation within the elastic deformation stage. The Zener's anisotropy index (*A*) was derived from equation (2):

$$A = \frac{2C_{44}}{C_{11} - C_{12}} \tag{2}$$

Finite element analysis for the developed unit cells and associated lattice structures were performed using the ABAQUS software. The strain-hardening elastoplastic behavior of LPBF fabricated *AlSi10Mg* alloy were determined using a tensile stress-strain curve obtained through experimental measurements. The mesh was generated employing the linear tetrahedral elements (C3D4) with an element size of 0.1 mm to balance efficiency and accuracy. The total number of elements enlisted were approximately 120,000, 150,000, and 230,000 for the RD, BCC, and OCTET structures, respectively. During the compression process simulation, the designed structures were placed between two rigid plates, and the load was applied by moving the rigid plates towards the center plane. The contact regions were assigned with a "hard" contact property. To accurately simulate the behavior of designed unit cells under compression, it was essential to consider the effects of geometric nonlinearity. This was achieved by enabling the 'NLGEOM' option within Abaqus, which facilitated the analysis of large displacements and rotations inherent in the system. The inclusion of geometric nonlinearity allowed for a more realistic representation of the mechanical interactions and highlighted critical stress concentrations that were not captured under linear modeling assumptions. Note that the simulation model was calibrated in our previous work [24], in which reasonable agreement between simulation and experimental results was achieved.

2.3. Material and LPBF fabrication

The fabrication of the tensile and lattice structure samples with the gas atomized AlSi10Mg alloy powders were conducted using the commercial EP-M150 LPBF machine. The optimized laser process parameters were determined as laser power of 370 w, laser scanning speed of 1300 mm/s, hatch distance of 110 μm and layer thickness of 30 μm. The above parameters guaranteed the fabricated bulk materials with high density of above 99.5%. Moreover, laser power and laser scanning speed for reducing down-surface roughness were selected as 260 W and 1300 mm/s, respectively. The fabricated 3 × 3 × 3 lattice structures with optimized unit cells can be seen in Figure 2.
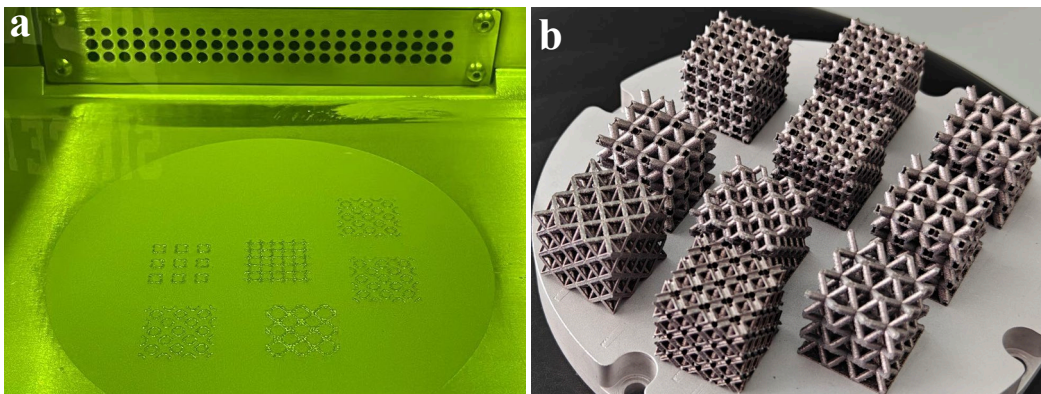

Figure 2. (a) LPBF building process and (b) the fabricated lattice structures.

2.4. Morphological characterization and mechanical property evaluation

The LPBF fabricated tensile and lattice structures were carefully cut off from the substrate using electrical discharge machining (EDM). The lattice structure samples were characterized by the Keyence VHX-7000 3D optical microscopy (OM) and the Zeiss Gemini 300 scanning electron microscopy (SEM), respectively. Before OM observation, the tapered hollow strut lattice structures were cleaned in alcohol under ultrasonic vibration to remove the residual powders.

The tensile properties of LPBF AlSi10Mg alloy were determined via tensile testing on a Shimadzu AG-IS 50 kN universal testing machine. The geometry of dog-bone shaped tensile samples can be found in [26]. At least three repeated experiments were conducted for each sample condition, and the test was performed by following the procedures in ASTM E8. Both the horizontally (sample tensile direction perpendicular to the building direction) and vertically (sample tensile direction parallel to the building direction) built samples were tested, and the Young's modulus was determined from the slope of the tested stress-strain curves within the elastic range. The uniaxial compression tests were performed to compare the mechanical performance of the developed lattice structures with its solid strut (without hollow in the strut of the studied lattice structure) and straight hollow strut (with straight hollow in the strut of the studied lattice structure) structure counterparts. Two samples for each condition were evaluated to confirm the data repeatability. The compression tests were conducted under a constant cross-head moving velocity of 2 mm/min, with the deformation process being recorded by a high resolution digital camera. The load-displacement data was recorded and then transferred to engineering stress-strain curves by dividing the effective cross-sectional areas and the lattice structure height, respectively.

3. Results

3.1. Tensile properties of LPBF fabricated AlSi10Mg alloy samples

Figure 3 shows the engineering stress-strain curves of the LPBF fabricated AlSi10Mg alloy samples build along vertical and horizontal directions. In general, the alloy demonstrated outstanding tensile properties as compared with its conventional casting counterparts, mainly due to the unique fine cellular microstructures within the LPBF generated molten pools [27]. Both the horizontal and vertical samples demonstrated similar yield strength. However, when compared to the vertical sample, the horizontal specimen displays marginally superior tensile strength alongside with a significantly enhanced elongation to fracture. Such mechanical property variance is mainly induced by the layer-wise molten pool configuration and the relatively lower strength in the heat affected zone along the molten pool boundary areas. The underlying mechanisms can be found in [28]. Moreover, no significant Young's modulus variance was observed between the two testing directions, and the determined yield strength and Young's modulus values were then used for guiding the following numerical simulations.
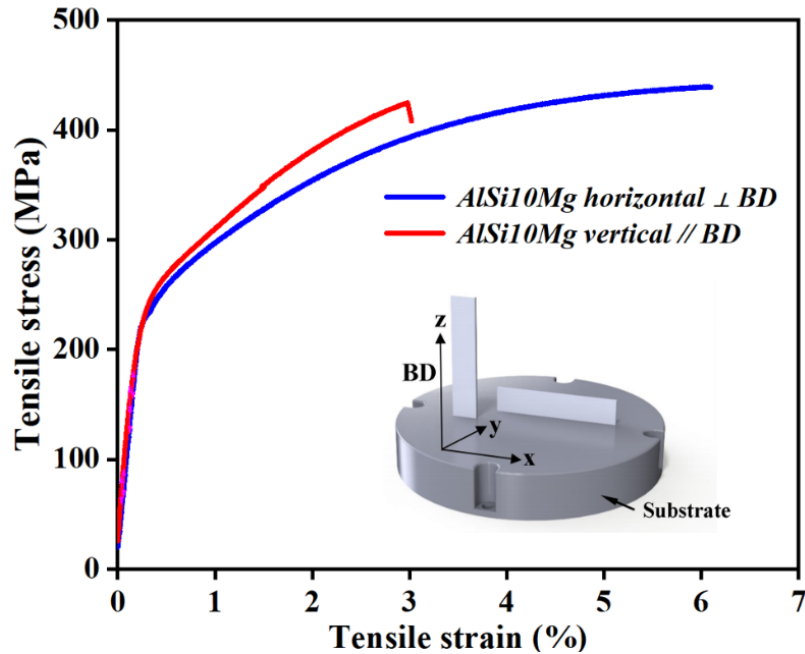
Figure 3. Tensile stress-strain curves of LPBF fabricated AlSi10Mg samples.

3.2. Numerical optimization of the designed unit cells

To achieve good combination between relative density, Young's modulus and isotropic mechanical properties, the finite element analysis was applied to evaluate the mechanical properties of the tapered hollow strut unit cells. The Young's modulus was derived as the slope of the elastic range of the stress-strain curve, while the yield strength was determined as the stress at 0.2% offset strain. The simulated physical properties including the relative density, Young's modulus and the Zener's anisotropy index as a function of geometric parameters r_{top} and r_{node} are summarized in Figure 4. Obviously, the relative density increased with the decrease of r_{top} and r_{node} for all the studied structures. The relative density is more sensitive to geometric parameters for the RD and the OCTET structures, while the BCC structure showed a balanced changing trend. This can result from the BCC structure topologies with large length-to-diameter ratio and less strut number. The Young's modulus, on the other hand, exhibited similar changing trend to the relative density, as there is a well-known Gibson-Ashby relationship between the relative density and the Young's modulus [29]. The Zener's anisotropy exhibited non-monotonic changing behaviors, and it varied significantly between different unit cell structures. Under the defined geometric parameters with a constant strut outer diameter of 2.6 mm, the Zener's anisotropy of BCC is much higher than RD and OCTET structures, indicating the tapered hollow strut design played minimal influence on reducing the anisotropy behavior of BCC structure in this case. The higher Zener's anisotropy value of the BCC structure can be attributed to its bending-dominated configuration as well as its low bearing capacity. The Zener's anisotropy increased with the simultaneous decrement of r_{top} and r_{node} values for the RD structure, while it also showed slight improvement at larger r_{top} and smaller r_{node} values. For the OCTET structure, it showed opposite changing trend to the RD structure, as it demonstrated the highest Zener's

anisotropy at larger r_{top} and smaller r_{node} values. Nevertheless, the above numerical simulation indicated that the mechanical isotropy (Zener's anisotropy equals to 1) can be achieved for the RD and OCTET structure by carefully tailoring the geometric parameters of the strut hollow structure.
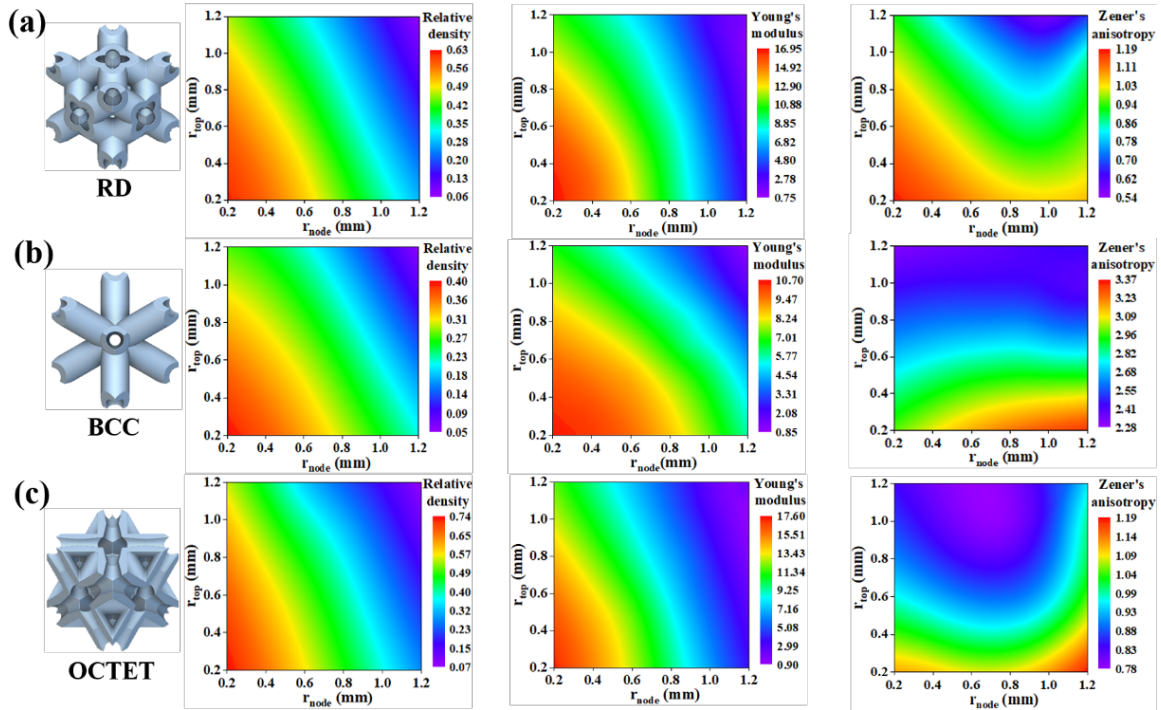

Figure 4. Relative density, Young's modulus and Zener's anisotropy properties of the designed tapered hollow strut structures as a function of geometric parameters for (a) RD structure, (b) BCC structure and (c) OCTET structure.

Apart from the above physical properties, the spatial resolution of LPBF fabricated aluminum lattice structure parts should also be emphasized, *i.e.* the effective strut wall thickness larger than 0.3 mm is generally required. Thus, to rationalize the geometrical configuration effect on properties of the developed unit cells, the radar map that displays the relative density, anisotropy, Young's modulus, strength and energy absorption are shown in Figure 5. It is worth noting that we mainly consider structures with relative density below 0.3 due to a) lightweight design requirements and b) higher relative density induced by smaller strut hollow diameters may cause powder residue issues within the printed hollow strut. Under the above premises, we now select the geometric configurations that demonstrates the most balanced performance. For the RD unit cell structure, though the hollow strut with top radius of 1 mm and node radius of 0.9 mm exhibited the best strength and energy absorption, it exhibited the worst Zener's anisotropy performance as compared with other configurations. By increasing the relative density of only 1.3%, the structure with tapered hollow strut of 0.7 mm top radius and 1 mm node radius (the blue line case) showed comparable mechanical performance but obviously enhanced isotropic mechanical properties. Due to the overall high Zener's anisotropy index value of the studied BCC unit cell structures, we selected the

tapered hollow strut with geometric parameters of top radius of 0.8 mm and node radius of 0.9 mm, as it possesses the relatively higher mechanical properties and acceptable relative density of 20.2%. On the other hand, as for the OCTET unit cell structure, the tapered hollow strut with top radius of 0.9 mm and node radius of 1 mm was selected mainly due to its lower density, though other parameters possessed higher mechanical performance. It is worth noting that the strut length of the optimized RD, BCC and OCTET structures are 3.464 mm, 6.928 mm and 5.657 mm, respectively. The above optimized unit cells will be assembled into the 3 × 3 × 3 lattice structures for LPBF fabrication, with the final aim of evaluating their mechanical properties as compared with their solid strut and straight hollow strut counterparts by experimental compression analysis. Previous studies have confirmed that the 3 × 3 × 3 type lattice structures are large enough to capture the periodicity and anisotropy in all three dimensions, which is also crucial for homogenization techniques used to predict the effective material properties [30].
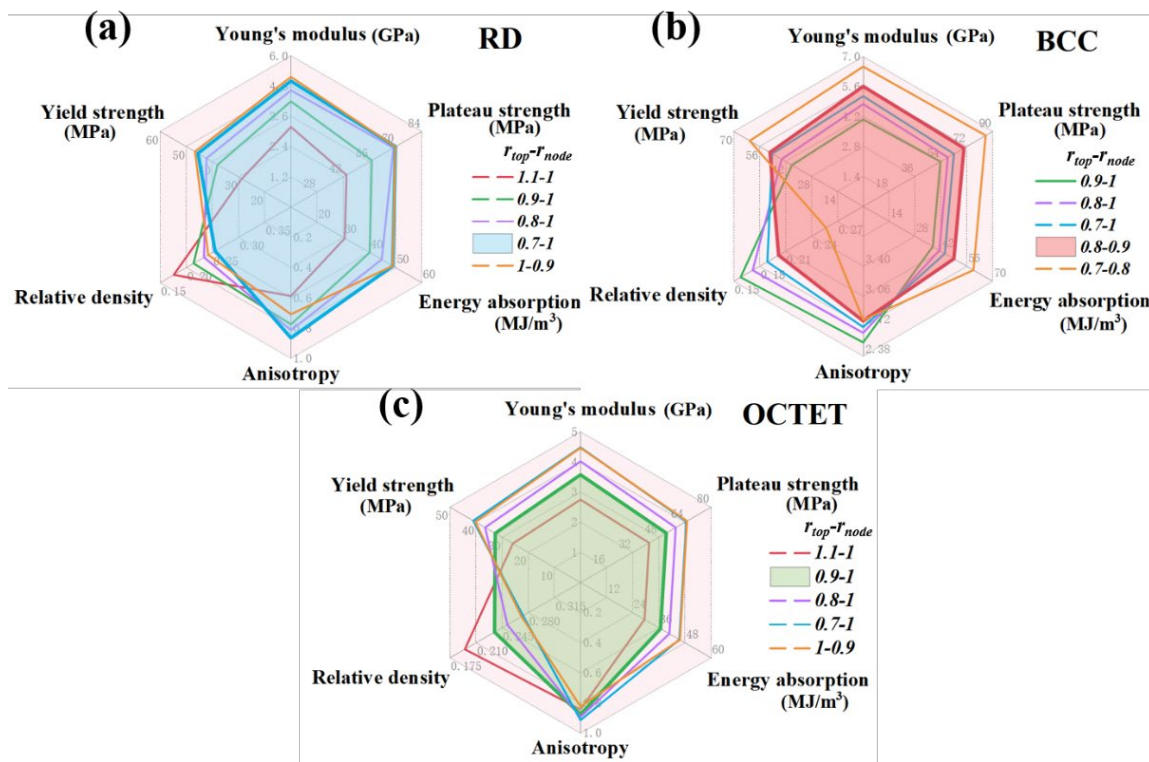

Figure 5. The radar map shows the physical and mechanical properties of (a) RD, (b) BCC and (c) OCTET unit cells with different tapered hollow strut geometric parameter designs.

3.3. Morphology observation of LPBF lattice structures

Figure 6 shows the macro-morphology of the LPBF fabricated lattice structures. In general, the LPBF lattice structures maintained good consistency and sound integrity as compared with their original CAD design (Figure 6a,d,g). Specifically, the strut hollow showed high uniformity while the node area of the lattice structure demonstrated acceptable formability

across different locations (Figure 6b,e). Moreover, the dashed lines in the OCTET lattice structure reflects the gradual wall thickness change, suggesting the high LPBF manufacturing quality in this study (Figure 6h,i). Though nearly no residual powder left inside the lattice structure, careful observation revealed the powder adhesion and dross defects located along the overhaning strut down-surface areas (Figure 6c,f). During the LPBF process, the lack of solid material support of overhaning structure may cause unstable molten pools as heat dissipation was largely inhibited on a powder bed, thus triggering the partially melted powders to adhere to the down-surface and form dross defects.
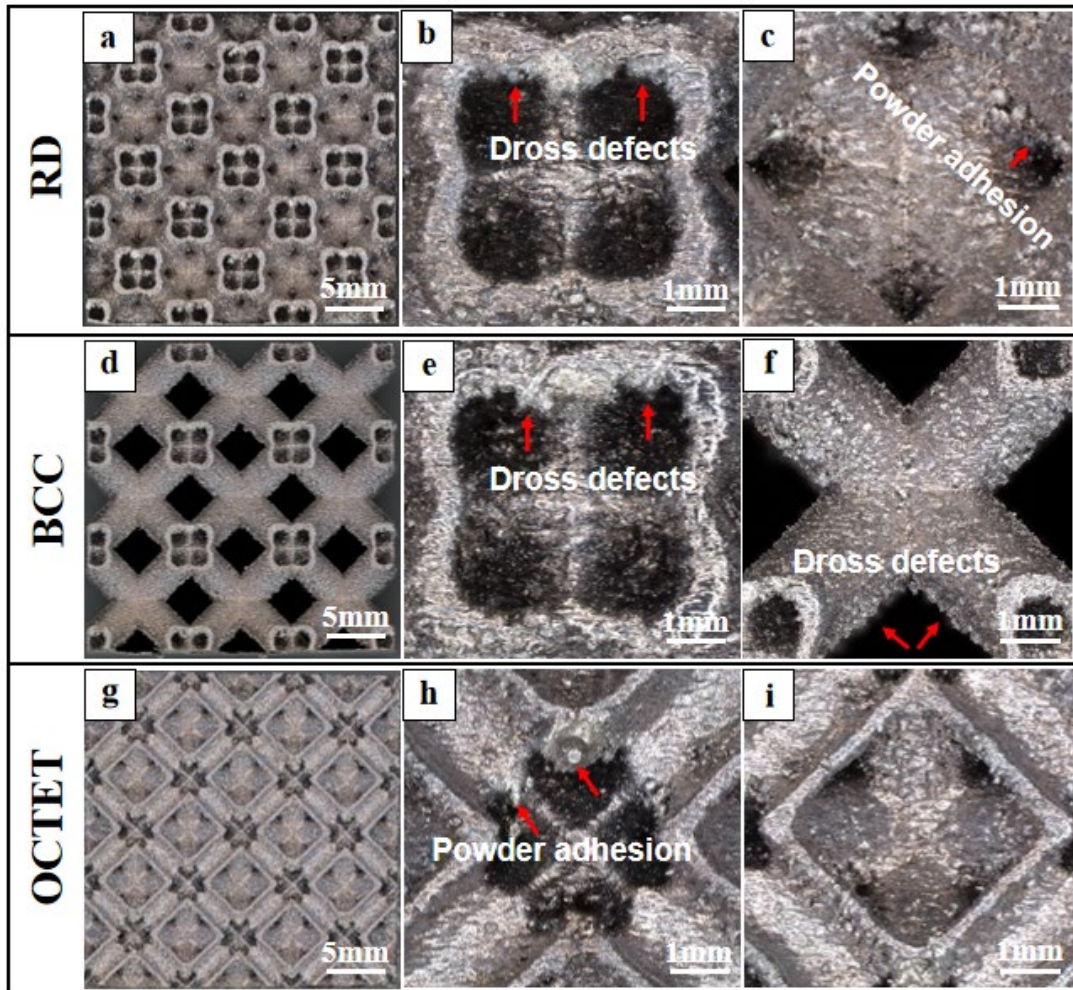

Figure 6. Macro-morphologies of LPBF (a-c) RD, (d-f) BCC and (g-i) OCTET lattice structures.

On the other hand, we performed SEM observation of the representative OCTET lattice structures at higher magnifications, especially for the micro-structure investigation of the tapered hollow strut design (Figure 7). Overall, as shown by the red circles, only several residual powders were observed to stick to the strut surface areas. From the top view, the step-like features are observed on the inclined strut up-surface areas, which may result from the unstable melt flow during the stacking of the molten pools (Figure 7a). Furthermore, as pointed by the red triangle symbols, rough surface caused by powder adhesion and dross

defects can also be observed for the inclined strut down-surface and the horizontal strut surface from the side view (Figure 7b). On the other hand, the hollow strut inner side also exhibited rough surface with step-like defects (Figure 7c). The above defects are commonly regarded as the main drawbacks of LPBF lattice structures, as they can pose a threat to the mechanical property consistency. Further quality improvement by either laser process parameter optimization and/or post treatment can be applied in future to remove the adhered powder and smooth the strut surface.
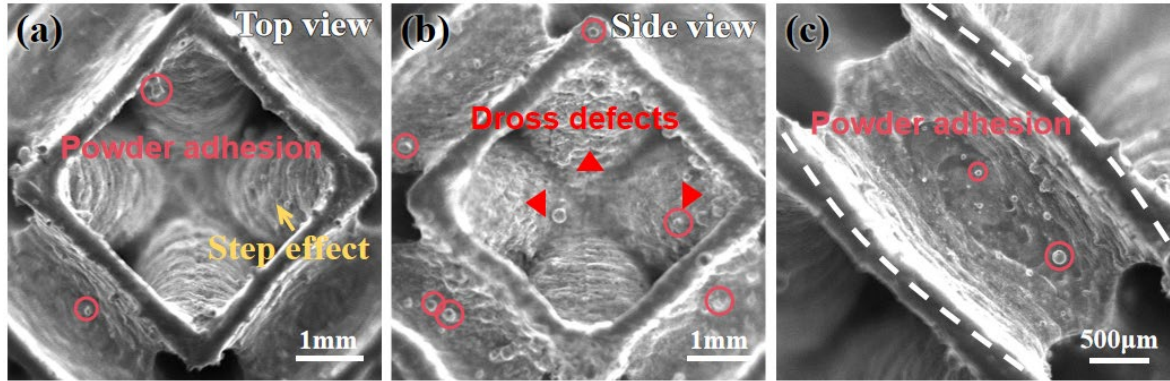

Figure 7. Typical microstructures of LPBF fabricated tapered hollow strut OCTET lattice structure from (a) top view, (b) side view and (c) inside the strut.

3.4. Mechanical performance of LPBF fabricated lattice structures

We now focus on the mechanical performance evaluation by experimental compression analysis of the developed lattice structures. Herein, the mechanical properties between the tapered hollow strut, the solid strut and the straight hollow strut lattice structures were compared under the same relative density. The mechanical properties were quantified by calculating the elastic modulus, the yield stress, the plateau stress and the energy absorption. In this study, the studied lattice structures (except the RD-solid lattice structure) experienced three typical deformation stages, *i.e.* the elastic-plastic stage, the stress fluctuation stage and the densification stage. Herein, the elastic modulus is determined by analyzing the slope of the compressive stress-strain curve within the elastic range, while the yield strength is defined as the stress at a plastic offset strain of 0.2%. The calculation for the plateau strength (σ_m) is given as [31]:

$$\sigma_m = \frac{1}{\varepsilon_2 - \varepsilon_1} \int_{\varepsilon_1}^{\varepsilon_2} \sigma d_\varepsilon \tag{3}$$

where ε_1 and ε_2 are the respective yield strain and densification strain, and σ is the compression stress. On the other hand, the energy absorption (EA), defined as the integral of the area under the compression stress-strain curve from zero strain to the onset strain (ε_d) of densification, quantifies the amount of energy a material can absorb under compressive loading. It can be expressed as [32]:

$$EA(\varepsilon) = \int_0^{\varepsilon_d} \sigma d\varepsilon \tag{4}$$
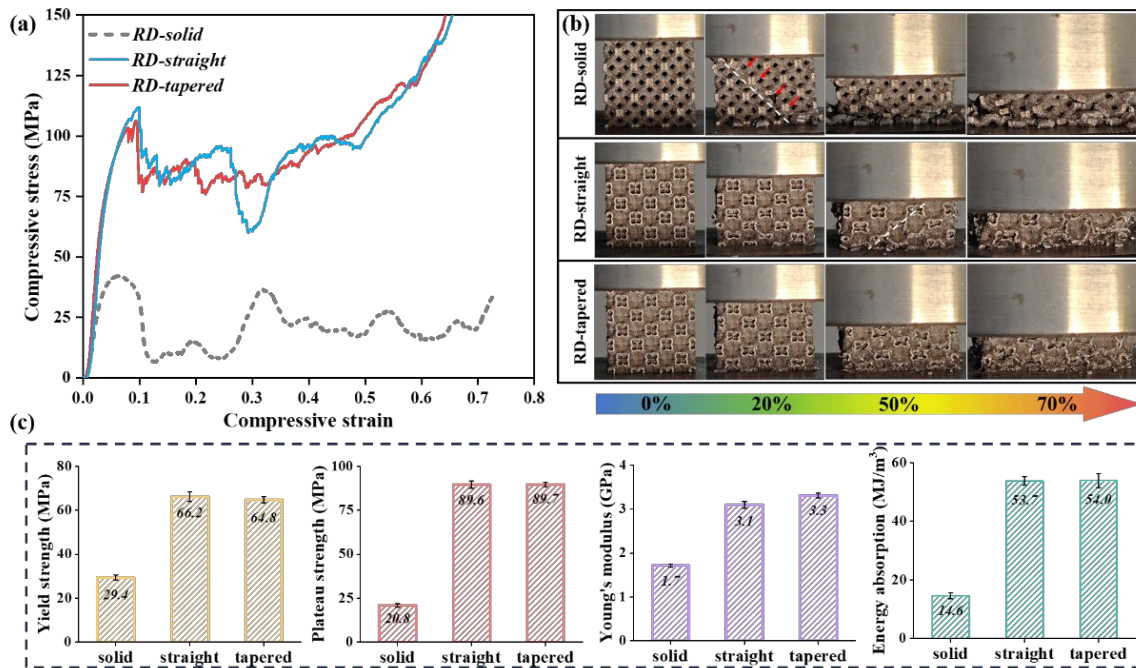
Figure 8. Compression results of LPBF fabricated RD lattice structure. (a) Compressive stress-strain curves, (b) compression deformation behaviors and (c) the calculated mechanical properties.

For the RD lattice structures, as can be seen in Figure 8a, the hollow strut samples exhibited more than doubled yield strength than the solid strut sample under the same relative density. The hollow strut lattice structures also displayed different stress fluctuation characteristics to the solid strut counterparts in the plateau stage, while the commonly observed densification stage due to local strut collapse was not observed in the latter case. Moreover, it can be seen that the tapered hollow strut lattice structure experienced milder stress fluctuations as compared with the straight hollow strut sample. Such distinct deformation characteristics suggesting the topological tapered hollow strut design indeed improved its deformation stability during the compression process. By careful analysis of the recorded deformation process (Figure 8b), we can easily observe the severe shear deformation along the diagonal direction of the solid strut lattice structure at only about 20% compressive strain. Afterwards, the RD-solid lattice structure experienced catastrophic brittle fracture, which well explains its lack of densification stage in the compressive stress-strain curve. On the other hand, only slight shearing behavior was observed at the compression strain of 50% for the RD-straight lattice structure. Interestingly, the shear deformation behavior of the RD-tapered lattice structure was basically suppressed, which helps it maintained the best shape integrity until fracture. As shown in Figure 8c, the tapered hollow strut lattice structure design enhanced the overall mechanical performance as compared with its solid strut counterparts for the RD lattice structure, while the tapered lattice structure shared similar mechanical properties with the hollow straight lattice structure.
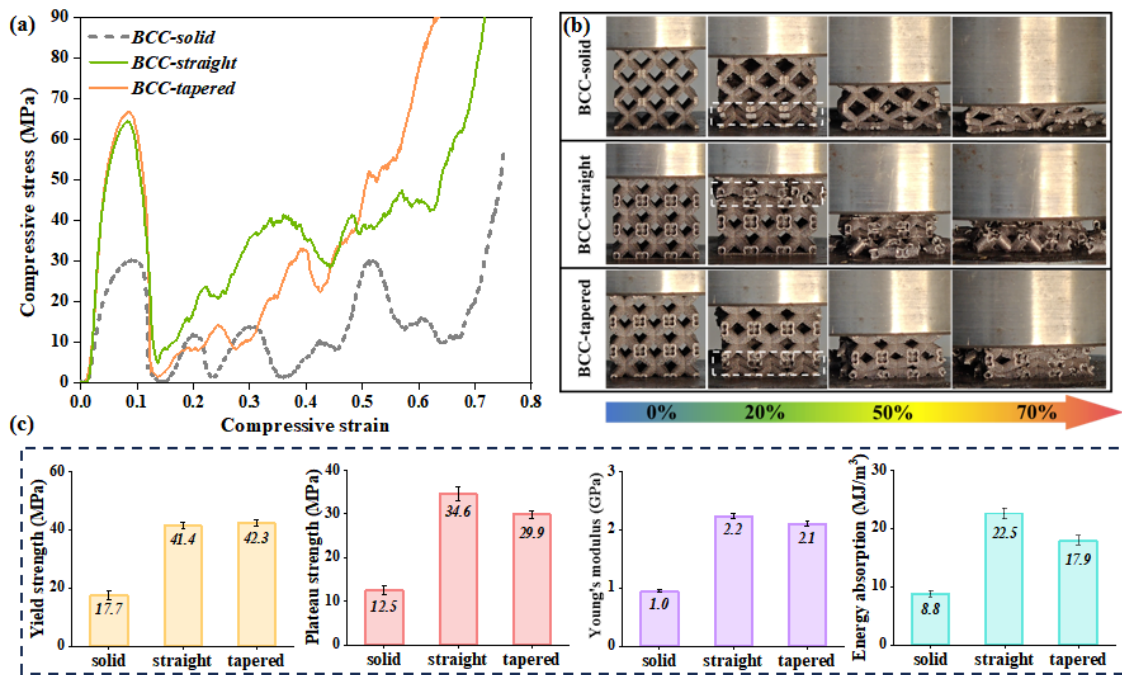
Figure 9. Compression results of LPBF fabricated BCC lattice structure. (a) Compressive stress-strain curves, (b) compression deformation behaviors and (c) the calculated mechanical properties.

Though the hollow strut design of the BCC lattice structure enhanced the overall mechanical performance as compared with the BCC solid strut lattice structure, the BCC-tapered lattice structure generally showed no obvious improvement of yield strength and Young's modulus to the BCC-straight lattice structure (Figure 9a). The compression process observation revealed that the LPBF BCC lattice structures all deformed in a layer-by-layer destruction manner, which explains the severe stress fluctuations in the compression stress-strain curves (Figure 9b). However, it still can be seen that the tapered hollow strut design performed relatively better deformation stability than those of two strut structures for up to at least 50% compression strain. Nevertheless, the tapered hollow strut design showed inferior plateau strength and energy absorption compared to the straight hollow strut lattice structure (Figure 9c).

As compared with the solid strut structure, the OCTET lattice structure design not only improved the mechanical properties, but also significantly alleviated the severe stress fluctuation behavior after yielding (Figure 10a). The excellent deformation stability of the hollow strut design was further confirmed by the recorded compression process, wherein different deformation characteristics were observed for the studied lattice structures (Figure 10b). The solid strut lattice structure showed two inclined 45° fracture feature after compression to 50% strain, while only several cracking sites were detected for the straight hollow strut structure. Similar to the RD lattice structures, the tapered hollow strut structure presented significantly better deformation stability, in which shearing and cracking behaviors were successfully inhibited. Moreover, as indicated by the white arrows, the tapered hollow strut experienced severe rotation, which reoriented its geometry relative to the applied load. This rotation

altered the effective load-bearing area by aligning more material to directly counteract the compressive force, thereby enhancing its ability to resist compression deformation. We suggest this might result from the increased bending and shear stiffness at the node regions of tapered hollow strut design, and the detailed underlying deformation mechanisms will be elucidated in the following section. Overall, the OCTET-tapered structure design presented better deformation stability but comparable mechanical performance to its straight hollow counterparts (Figure 10c).
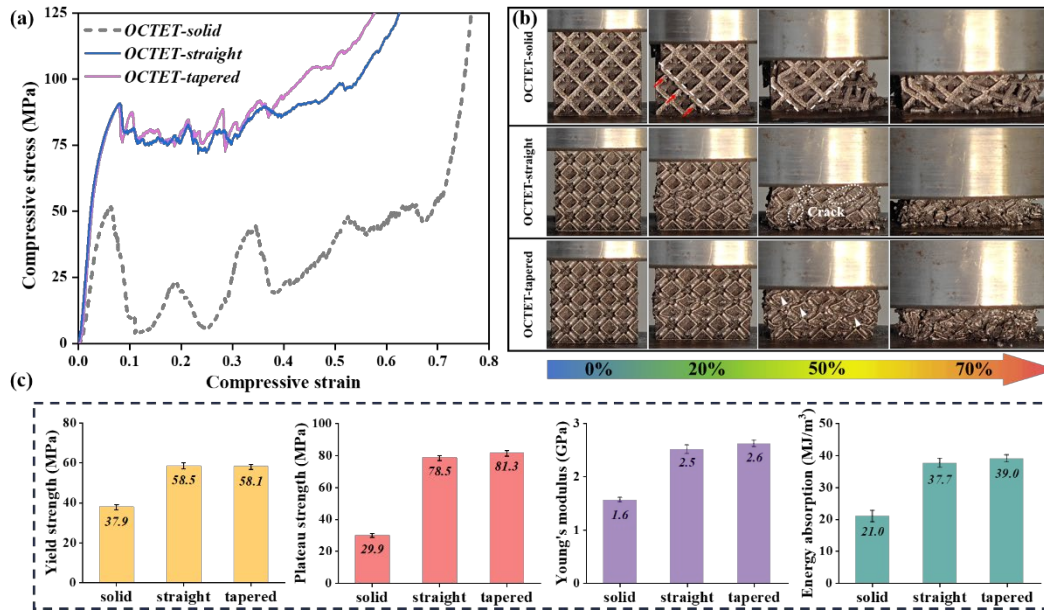

Figure 10. Compression results of LPBF fabricated OCTET lattice structure. (a) Compressive stress-strain curves, (b) compression deformation behaviors and (c) the calculated mechanical properties.

3.5. Deformation modes analysis

An exploration of the compressive deformation processes of the studied lattice structures has been undertaken to understand the intrinsic deformation modes and their effect on compressive properties. Previously, the Gibson-Ashby model has been applied to evaluate the deformation behavior modes of lattice structures, which normally categorized the deformation mechanism of lattice materials into bending-dominated and stretching dominated. However, the above model (fundamentally based on the Euler-Bernoulli beam theory [29]) is only applicable when length-to-diameter ratio of strut exceeds 5. Given all strut ratios in our optimized lattice structures are less than 5, *i.e.* RD = 1.332, BCC = 2.665, OCTET = 2.176, the applicability of the Gibson-Ashy model becomes limited in this study. For such reason, we employ Timoshenko beam theory (feasible to strut length-to-diameter ratio less than 5) to concurrently investigate the stretching, bending, and shear deformation behaviors of the struts.

Take the BCC unit cell as an example, the upper half part of which comprises four equally inclined struts, and each strut is subject to a force (F_{strut}) when a compression is

applied along the Z direction. The strut displacement generated by each deformation mechanism can be generally written as [31]:

$$\delta_{strut}^{streching(z)} = \frac{lF_{strut}\sin^2\theta}{AE_s} \tag{5}$$

$$\delta_{strut}^{bending(z)} = \frac{l^3F_{strut}\cos^2\theta}{12E_sI} \tag{6}$$

$$\delta_{strut}^{shear(z)} = \frac{lF_{strut}(2+2v)\cos^2\theta}{A\kappa E_s} \tag{7}$$

Herein, A is the effective cross-sectional area of the strut, k is the shear coefficient, v is the Poisson's ratio of the material, I is the moment of inertia and E_s is the Young's modulus of the material. The force F_{strut} can be resolved into two components: one in the direction parallel to the strut $F_{strut}\sin\theta$ and the other perpendicular to $F_{strut}\cos\theta$ it. The length of the strut is $4\sqrt{3}$ mm. Given that both the strut length and the relative density remain constant, the cross-sectional area (A) remains invariably unchanged from solid to hollow struts (2.96 mm^2). It shifts from 2.763 to 3.297 mm^2 as the inner radius decreased from 0.9 to 0.8 mm in the tapered hollow strut. The second moment of inertia (I) are 0.425 and 1.804 mm^4 for the solid and straight hollow strut structure, respectively, while it ranged from 1.727 to 1.921 mm^4 for the tapered hollow strut structure.
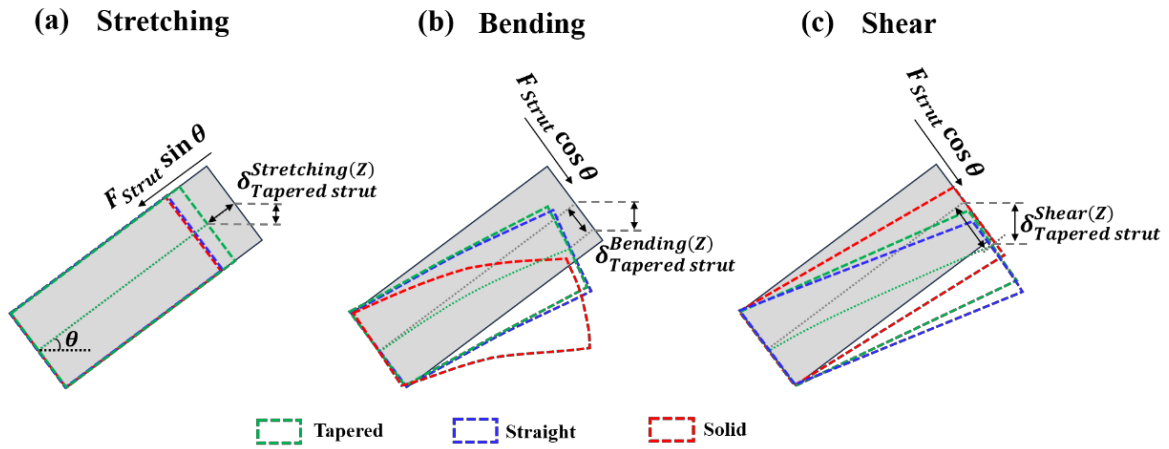

Figure 11. Illustration of the tapered hollow strut, straight hollow strut and solid strut under (a) stretching, (b) bending and (c) shear.

As illustrated in Figure 11, for the solid strut, the calculated bending deformation $\delta_{bending}$ surpassed both shearing ($\delta_{shearing}$) and stretching ($\delta_{stretching}$) deformations, indicating that the solid strut is a bending-dominated structure under the compressive load. In contrast, in the straight and tapered hollow struts, $\delta_{bending}$ marginally overpowers $\delta_{shearing}$, but remains significantly larger than $\delta_{stretching}$. It suggests that the dominated deformation mechanism becomes a mixed mode of bending and shear due to the internal hollow structure. Moreover, compared to the straight and tapered hollow structures, the calculated bending deformation of the solid strut is nearly 5 times larger than those of the straight and tapered hollow structure

due to the smaller *I*. Subsequently, the bending strength of the hollow strut structure increases. On the other hand, the higher shear coefficient (*k*) of solid strut (k_{solid} = 0.889, $k_{straight}$ = 0.567 *and* 0.561 < $k_{tapered}$ <0.580) provides higher shear resistance, resulting in smaller shear deformation. However, compared to the significant increase in the bending deformation from solid strut to straight hollow strut and tapered hollow strut, the decrease in the shear deformation is negligible. This is because the hollow struts, despite having a higher shear coefficient, still experience a substantial increase in bending deformation due to the reduction in the moment of inertia [32]. Therefore, we can now conclude that the straight and tapered hollow struts are stronger and stiffer than solid struts, which explains why the corresponding lattice structures possessed higher yield strength and higher elastic modulus.

Compared with the straight hollow strut, the inner diameter of the tapered hollow strut decreased linearly from the middle cross section towards two opposite ends. Concurrently, the increase in wall thickness enhanced the bending and shear load carrying capacity, while the resistance at the middle of the strut became weakened. Research findings indicate that the Misses stress mainly concentrates at the node regions when lattice structures are subject to compression deformation [33]. Such phenomenon was also found in the simulated maximum principle true strain distribution of the RD, BCC, and OCTET structures in this study (Figure 12).
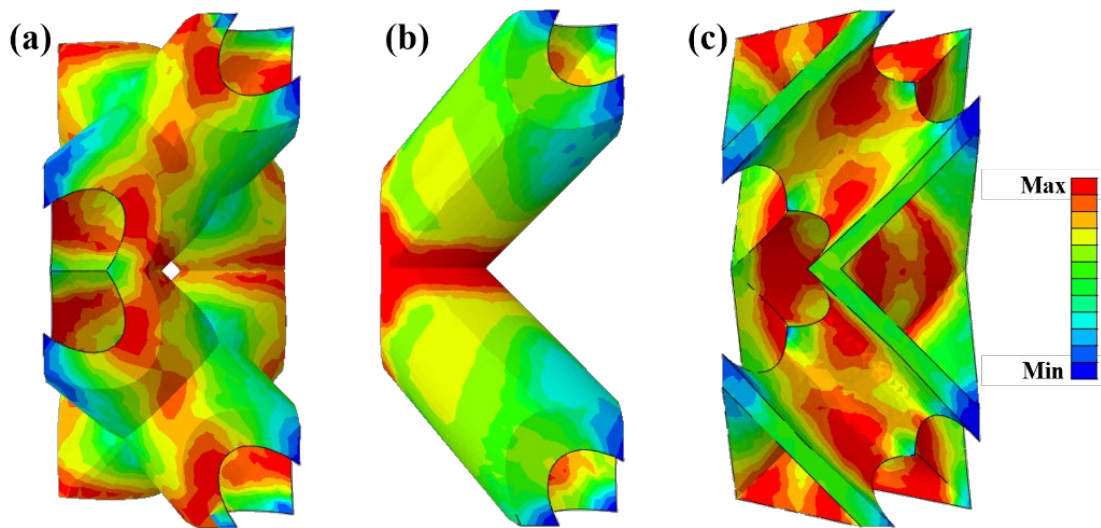

Figure 12. Mises stress distribution of tapered hollow strut (a) RD, (b) BCC and (c) OCTET unit cells under uniaxial compression with symmetric boundary conditions.

Thanks to the increased wall thickness in the node regions, the tapered hollow lattice structure exhibited a localized enhancement in its load-bearing capacity as compared with its straight hollow counterpart. Such enhancement contributed favorably to the structural integrity, which explains the different deformation behavior between the hollow and tapered hollow strut lattice structures. Despite severe bending deformation for the tapered hollow struts, the RD and OCTET lattice structure overall maintained sound integrity as compared with its straight hollow strut counterparts, where shear deformation and cracks were observed once the compressive strain increased to 0.5 (Figure 8b and 10b). This discrepancy also indicates the better shear resistance of the RD-tapered and OCTET-tapered hollow strut

lattice structures around the node region, which aligns well with the relatively milder stress fluctuations in the corresponding stress-strain curves. As for the BCC structure, all samples visibly exhibited a progressive layer collapse once the stress around the node region exceeded the ultimate strength, which might be attributed to the specific topology feature of BCC structure, especially for its excessive strut length and less node numbers.

4. Conclusion

In this study, the tapered hollow strut lattice structure design strategy was extended to other typical lattice structures. The mechanical performance and deformation modes of such structures were analyzed. The main findings can be concluded as follows:

(1) To achieved a balanced property between relative density, mechanical performance and LPBF processability, the geometric parameters of the tapered hollow strut were optimized to be $r_{top} = 0.7$ mm and $r_{node} = 1$ mm for RD structure, $r_{top} = 0.8$ mm and $r_{node} = 0.9$ mm for BCC structure and $r_{top} = 0.9$ mm and $r_{node} = 1$ mm for OCTET structure, respectively.

(2) Experimental compression analysis showed that the hollow strut design can significantly enhance the mechanical properties, while the tapered hollow strut designed improved the deformation stability as compared with its straight hollow strut and solid strut counterparts.

(3) Deformation modes analysis revealed that the increased wall thickness around the node regions of the tapered hollow strut design enhanced the shear and bending resistant capacity of the lattice structures, which explains its enhanced deformation stability.

Conflicts of interests

The authors declare that they have no known competing financial interests or personal relationships that could have appeared to influence the work reported in this paper.

Authors' contribution

Y.Song: Investigation, Data curation, Formal analysis, Software. **Z.Y. Chen:** Investigation, Formal analysis, Software. **T.Z. Wei:** Investigation, Formal analysis. **C. Ge:** Investigation, Data curation. **Y.A. Cheng:** Investigation, Formal analysis. **M. Liu:** Writing-review & editing, Investigation, Formal analysis, Data curation, Methodology. **Q.B. Jia:** Writing-review & editing, Supervision, Resources, Funding acquisition, Methodology, Conceptualization.

References

[1] Zadpoor AA. Mechanical performance of additively manufactured meta-biomaterials. *Acta Biomater.* 2019, 85:41–59.

[2] Maconachie T, Leary M, Lozanovski B, Zhang X, Qian M, *et al.* SLM lattice structures: Properties, performance, applications and challenges. *Mater. Des.* 2019, 183:108137.

[3] Li Q, Tian W, Wu D, Gao W. Nonlinear dynamic stability analysis of imperfect architected cellular sandwich plate under impact loading. *Acta Mech. Sin.* 2023, 39(4):722333.

[4] Yeo SJ, Oh MJ, Yoo PJ. Structurally controlled cellular architectures for high-performance ultra-lightweight materials. *Adv. Mater.* 2019, 31(34):1803670.

[5] Tian W, Li Q, Wang Q, Chen D, Gao W. Additive manufacturing error quantification on stability of composite sandwich plates with lattice-cores through machine learning technique. *Compos. Struct.* 2024, 327:117645.

[6] Zhang L, Song B, Fu JJ, Wei SS, Yang L, *et al.* Topology-optimized lattice structures with simultaneously high stiffness and light weight fabricated by selective laser melting: Design, manufacturing and characterization. *J. Manuf. Processes* 2020, 56:1166-1177.

[7] Tancogne-Dejean T, Spierings AB, Mohr D. Additively-manufactured metallic micro-lattice materials for high specific energy absorption under static and dynamic loading. *Acta Mater.* 2016, 116:14–28.

[8] Qi D, Yu H, Liu M, Huang H, Xu S, *et al.* Mechanical behaviors of SLM additive manufactured octet-truss and truncated-octahedron lattice structures with uniform and taper beams. *Int. J. Mech. Sci.* 2019, 163:105091.

[9] Xiao L, Xu X, Feng G, Li S, Song W, *et al.* Compressive performance and energy absorption of additively manufactured metallic hybrid lattice structures. *Int. J. Mech. Sci.* 2022, 219:107093.

[10] Zhang S, Yang F, Li P, Bian Y, Zhao J, *et al.* A topologically gradient body centered lattice design with enhanced stiffness and energy absorption properties. *Eng. Struct.* 2022, 263:114384.

[11] Wang C, Vangelatos Z, Grigoropoulos CP, Ma Z. Micro-engineered architected metamaterials for cell and tissue engineering. *Mater. Today Adv.* 2022, 13:100206.

[12] Li X, Yu X, Zhao M, Li Z, Wang Z, *et al.* Multi-level bioinspired microlattice with broadband sound-absorption capabilities and deformation-tolerant compressive response. *Adv. Funct. Mater.* 2023, 33(2):2210160.

[13] Xu Z, La Mendola I, Razavi N, Bagherifard S. Additive manufactured Triply Periodical Minimal Surface lattice structures with modulated hybrid topology. *Eng. Struct.* 2023, 289:116249.

[14] Sharma D, Hiremath SS. Bio-inspired repeatable lattice structures for energy absorption: Experimental and finite element study. *Compos. Struct.* 2022, 283:115102.

[15] Jia Z, Chen H, Deng Z, Li L. Architected microlattices for structural and functional applications: Lessons from nature. *Matter* 2023, 6(4):1082–1095.

[16] Kumar A, Collini L, Daurel A, Jeng J-Y. Design and additive manufacturing of closed

cells from supportless lattice structure. *Addit. Manuf.* 2020, 33:101168.

[17] Li Q, Xiao M, Wang D, Wu Y, Liu K, *et al.* Energy absorption characteristics of starfruit-inspired biomimetic lattice structure under non-axial compression loading. *Eng. Struct.* 2023, 294:116767.

[18] Li Z, Chen C, Mi R, Gan W, Dai J, *et al.* A strong, tough, and scalable structural material from fast-growing bamboo. *Adv. Mater.* 2020, 32(10):1906308.

[19] Sun H, Li H, Dauletbek A, Lorenzo R, Corbi I, *et al.* Review on materials and structures inspired by bamboo. *Constr. Build. Mater.* 2022, 325:126656.

[20] Zou M, Xu S, Wei C, Wang H, Liu Z. A bionic method for the crashworthiness design of thin-walled structures inspired by bamboo. *Thin-Walled Struct.* 2016, 101:222–230.

[21] Hu D, Wang Y, Song B, Dang L, Zhang Z. Energy-absorption characteristics of a bionic honeycomb tubular nested structure inspired by bamboo under axial crushing. *Composites, Part B* 2019, 162:21–32.

[22] Zhao M, Li X, Zhang DZ, Zhai W. Geometry effect on mechanical properties and elastic isotropy optimization of bamboo-inspired lattice structures. *Addit. Manuf.* 2023, 64:103438.

[23] Li Q, Wu L, Hu L, Chen T, Zou T, *et al.* Axial compression performance of a bamboo-inspired porous lattice structure. *Thin-Walled Struct.* 2022, 180:109803.

[24] Ge J, Song Y, Chen Z, Zhuo Y, Wei T, *et al.* Effect of geometrical parameters on the mechanical performance of bamboo-inspired gradient hollow-strut octet lattice structure fabricated by additive manufacturing. *Micromachines* 2024, 15(583):1–14.

[25] Bonatti C, Mohr D. Large deformation response of additively-manufactured FCC metamaterials: From octet truss lattices towards continuous shell mesostructures. *Int. J. Plast.* 2017, 92:122–147.

[26] Chen Z, Chen A, Jia Q, Xia Z, Li R, *et al.* Investigation of microstructures and strengthening mechanisms in an N-doped Co-Cr-Mo alloy fabricated by laser powder bed fusion. *Virtual Phys. Prototy.* 2023, 18(1):e2219665.

[27] Thijs L, Kempen K, Kruth J-P, Van Humbeeck J. Fine-structured aluminium products with controllable texture by selective laser melting of pre-alloyed AlSi10Mg powder. *Acta Mater.* 2013, 61(5):1809–1819.

[28] Santos Macías JG, Douillard T, Zhao L, Maire E, Pyka G, *et al.* Influence on microstructure, strength and ductility of build platform temperature during laser powder bed fusion of AlSi10Mg. *Acta Mater.* 2020, 201:231–243.

[29] Gibson LJ, Ashby MF. *Cellular solids structure and properties*, 2nd ed. Cambridge: Cambridge University Press, 1997.

[30] Yeo SJ, Oh MJ, Yoo PJ. Structurally controlled cellular architectures for high-performance ultra-lightweight materials. *Adv. Mater.* 2019, 31(34):1803670.

[31] Wang Z, Cao X, Yang H, Du X, Ma B, *et al.* Additively-manufactured 3D truss-lattice materials for enhanced mechanical performance and tunable anisotropy: Simulations & experiments. *Thin-Walled Struct.* 2023, 183:110439.

[32] Zhong HZ, Song T, Li CW, Das R, Gu JF, *et al.* Understanding the superior mechanical properties of hollow-strut metal lattice materials. *Scripta Mater.* 2023, 228:115341.

[33] Zhang Z, Zhang L, Song B, Yao Y, Shi Y. Bamboo-inspired, simulation-guided design and 3D printing of light-weight and high-strength mechanical metamaterials. *Appl. Mater. Today* 2022, 26:101268.